

Respiratory Motion Modelling

Antonio Remiro Azócar, MSc Machine Learning

April 15, 2017

Abstract: 18 different respiratory motion models have been reviewed and implemented. These motion models relate the respiratory motion of the internal anatomy to an easy-to-measure surrogate signal. Model performance has been evaluated using visual assessment, deformation field error, landmark errors and uncertainty estimation. The advantages, disadvantages and future scope of the implemented techniques is discussed.

1 Introduction

Respiratory motion causes problems in the domains of image acquisition and image guided intervention in the thorax and abdomen. In image acquisition, it introduces artefacts which degrade the quality of reconstructed images [1,2]. In image guided intervention, it limits the accuracy of the guidance, triggering misalignments between static guidance data and the moving anatomy [3]. Current approaches to counteract the respiratory motion problem include breath-holding, respiratory gating and motion tracking e.g. via X-ray [4]. The first method potentially limits acquisition times to under 30s; this is problematic in many contexts. The second method involves acquiring imaging data for a limited target region; this increases intervention times overall. Motion tracking enables obtaining accurate knowledge of the motion of the internal anatomy. However, it is an invasive approach, requiring internal marker implantation for tracking, and in addition, limiting data capture to only a specific region of interest.

Respiratory motion models have been proposed as solutions to the aforementioned drawbacks. These correspondence models relate the motion of a patient's internal anatomy to a respiratory surrogate signal [5-9]. This signal is generally easy to monitor and may be provided by spirometry or by the displacement of a skin surface e.g. the height of a patient's chest or abdomen. Figures 1 and 2 demonstrate how correspondence models are used. Figure 1 highlights the model building process, occurring prior to radiotherapy treatment. Initially, imaging data is acquired simultaneously with the surrogate signal(s). The motion of the internal anatomy is provided by the imaging data; the correspondence model fitting such motion to the signal measurements. Figure 2 shows how the model is used during treatment, estimating the internal motion from the monitored surrogate signal(s). These estimates could potentially be used to plan and guide gated or tracked treatments [10]. In addition, they could be utilised to monitor delivery and help facilitate adaptive radiotherapy [11].

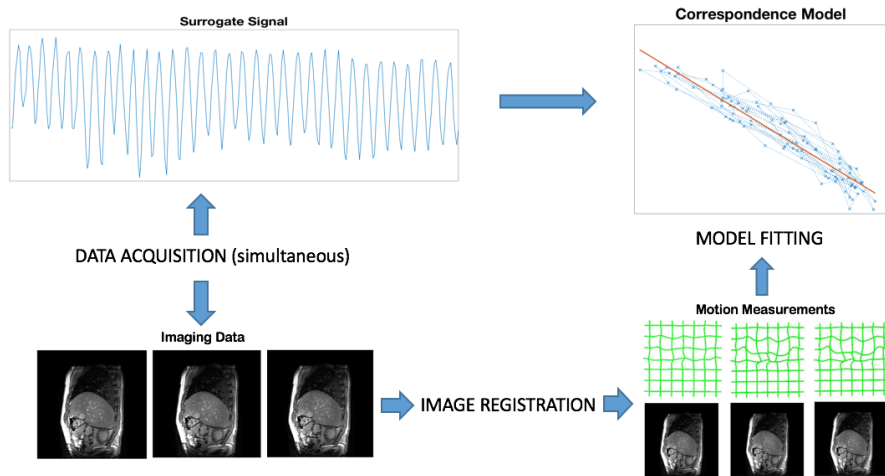


Figure 1: **Model building.** (i) Imaging data and the surrogate signal(s) are acquired simultaneously. (ii) Respiratory motion information is obtained from the imaging data via image registration. (iii) A correspondence model fits the motion to the surrogate signal(s). The deformation grids have been obtained from [6].

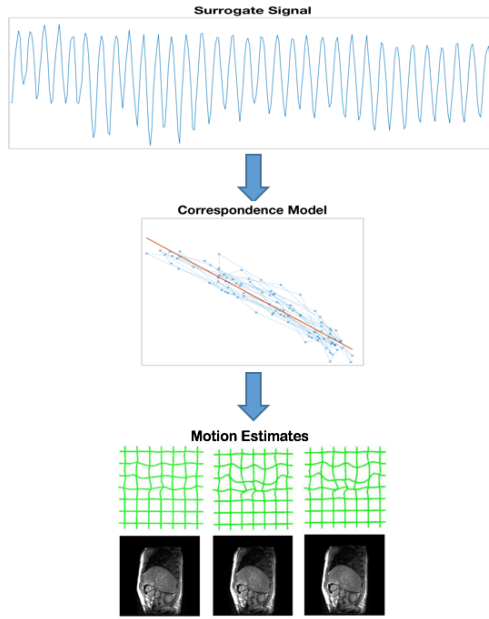


Figure 2: **Model usage.** (i) During treatment, the surrogate signal(s) is easy to measure. (ii) The correspondence model is used to estimate the motion of the internal anatomy from the surrogate signal measurements.

In Figure 1, the data used for model building must be acquired fast enough to ‘freeze’ the respiratory motion. On the other hand, in Figure 2, the image acquisitions where the models are used to compensate for the motion can be much slower.

2 Data and Modelling

A respiratory motion model is generally categorised by three components: the surrogate, the representation of internal motion, and the mathematical formulation used to relate both.

2.1 Data

Perhaps the biggest challenge when constructing a model for respiratory motion is acquiring the appropriate imaging data. For this project, both the respiratory surrogate signal and the motion of the internal anatomy have been measured from 2D+ t multi-slice sagittal MRI data. MRI data has been used in previous literature to build correspondence models [12-14]. It has the advantage of not exposing the patient to ionising radiation, potentially allowing for the collection of more imaging data (capturing both intra-fraction and inter-fraction variation) and enabling volunteer studies. As the image data is 2D, only 2D motion can be modelled. This is not problematic since generally, most of the motion of the lungs is captured by the Anterior-Posterior (AP) and Superior-Inferior (SI) directions (the sagittal plane). In addition, 2D data provides a necessary compromise for imaging with sufficiently high spatial and temporal resolution. Acquiring 3D volumes of the lungs at a fast enough temporal resolution (e.g. 0.5 seconds per image) is only achieved at the expense of poor spatial resolution/image quality [12,13].

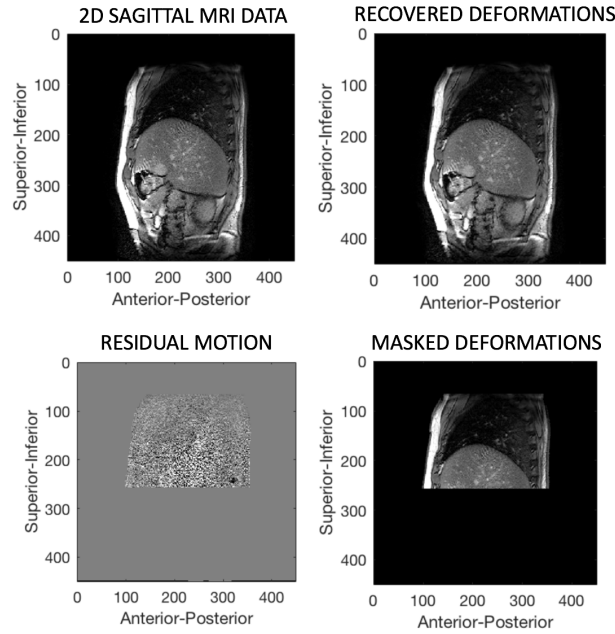
The MRI dataset consists of multi-slice data acquired from one healthy volunteer during free-breathing. The dataset is composed of 300 images in NIfTI format acquired at approximately 5fps. The slices are 10mm thick, with an in-slice resolution of $0.9375\text{mm} \times 0.9375\text{mm}$. A respiratory surrogate signal is generated from the AP displacement of the subject’s skin surface (as seen in the MRI data). Note that even though, in this case, the surrogate signal is generated from the MRI data, one can also measure a similar signal using other devices e.g. surface imagers, belts, markers, during an image acquisition. The 300 images acquired cover over 30 respiratory cycles, enough to sample inter-cycle variations for the subject. Unfortunately, the imaging data was collected during a single fraction (treatment session). Hence, inter-fraction variations are not evaluated in this study. .

The respiratory motion has been estimated from the MRI data using B-spline deformable image registration. The registration results are stored as a series of B-spline transformations i.e. deformations of a regular Control Point (CP) grid. These result from registering every MR image to a reference image: the first image acquired at the end of exhalation. The registration results are stored as 5D NIfTI images, with singular 3rd and 4th dimensions and a 5th dimension of size 2 containing the deformed location of the CP. In addition, this study also makes use of anatomic landmark data to evaluate the quality of the motion models and registrations. This data has been obtained via template tracking and consists of the coordinates of three anatomical landmarks

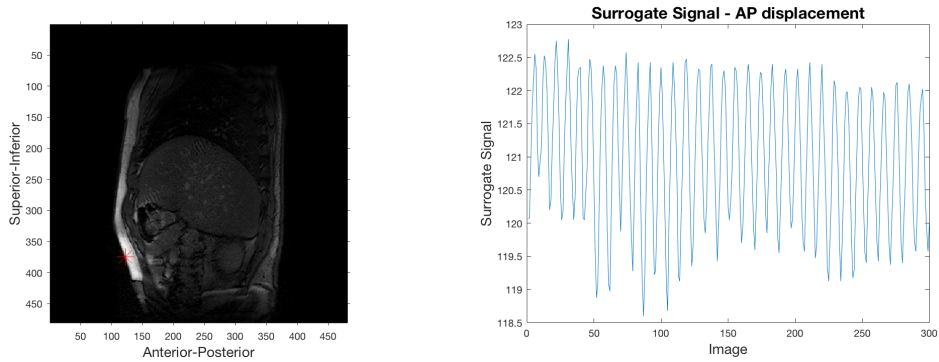
(blood vessels) for every image. Finally, a deformation field mask is utilised to disregard areas of the MR images with no respiratory motion when calculating the deformation field error. This will be discussed in a subsequent section.

Figures 3-6 eyeball how the MRI data is used in this study. Figure 3 presents a loaded MR image from the dataset. Figure 4 displays the B-spline deformations obtained from the registration results for the corresponding image. Figure 5 shows the differences between the deformations and the reference image used for the registrations over the provided ‘mask’ area. This figure provides a representation of the residual motion not recovered by the registrations in the results. As we can observe, the registrations are not perfect, with image artefacts occurring due to motion in and out of the sagittal plane. Figure 6 presents the deformations from Figure 4 but only over the ‘mask’ area. Notice how the ‘mask’ ignores the pixels outside the body (where there should be no motion) and below the liver (where there is motion but not caused by respiration). Linear interpolation is utilised to estimate this point to sub-pixel accuracy.

Figures 7 and 8 illustrate how the surrogate signal is generated. In this example, the surrogate signal is generated by finding the AP location of the skin surface at SI= 375 pixels in each of the images. Such location is estimated by locating the first point in the image with an intensity of 70 when coming from the anterior side. Figure 7 highlights the location of the skin surface at SI= 375 pixels with a red asterisk. Figure 8 shows a plot of the generated surrogate signal over each image.



Figures 3-6 (top left to bottom right). Figure 3: 2D sagittal MR image for the subject. Figure 4: Mapping of B-spline deformations obtained from the registration results for the corresponding image. Figure 5: Residual motion over the provided ‘mask’ area, representing the motion not recovered by the registrations. Figure 6: Recovered deformations from Figure 4 but only over the ‘mask’ area.



Figures 7 and 8 (left to right). Figure 7: 2D sagittal MR image highlighting the location of the skin surface at SI= 375 pixels. Figure 8: Plot of the generated surrogate signal (AP displacement) over each MR image.

2.2 Modelling

2.2.1 Theory and methodology

The points discussed in previous sections will now be formulated mathematically. As mentioned previously, we have a set of image data consisting of $N_i = 300$ dynamic images, $\mathbf{I}_1, \dots, \mathbf{I}_{N_i=300}$. Each image characterises a certain respiratory state at a different time point t . As discussed in 2.1, a reference image from the dataset, denoted \mathbf{I}_0 , is registered to each of the dynamic images \mathbf{I}_t , thus providing the respiratory motion data. Each registration is executed independently and produces a spatial transformation parametrised by motion parameters $\mathbf{M}_t = [m_{t,1}, \dots, m_{t,N_m}]$, where N_m is the number of motion parameters (the number of data points/anatomical landmarks being modelled). In this case, \mathbf{M}_t represents control point grids defining B-spline transformations. Formally, a correspondence model for respiratory motion is formulated as:

$$\mathbf{M}_{F_t} = F(\mathbf{S}_t, \mathbf{R}), \quad (1)$$

where F is a function of the surrogate data $\mathbf{S}_t = [s_{t,1}, \dots, s_{t,N_s}]$, where N_s is the number of surrogate signals measured at a time point t . The number and nature of the surrogate data determines the number of degrees of freedom of the model. F is also a function of model parameters $\mathbf{R} = \mathbf{R}_1, \dots, \mathbf{R}_{N_r}$, where N_r is the number of model parameters per motion parameter. Notice that the total number of model parameters is $N_r \times N_m$ i.e. we have $\mathbf{R} = [r_{1,n}, \dots, r_{N_m,n}]$. In equation (1), the correspondence model results in a vector of motion parameter estimates $\mathbf{M}_{F_t} = [m_{F_t,1}, \dots, m_{F_t,N_m}]$.

The following components characterise our respiratory motion model:

- The choice of surrogate data, i.e. \mathbf{S}_t in equation (1); which signals are input to the model?
- The correspondence model: how does the motion representation i.e. F in equation (1), relate to the surrogate data. How is the relationship parametrised?
- The model fitting procedure: how one determines F when fitting the correspondence model to the training data.

The next three subsections explore the choices made relating to the above components.

2.2.2 Choice of input surrogate signal(s)

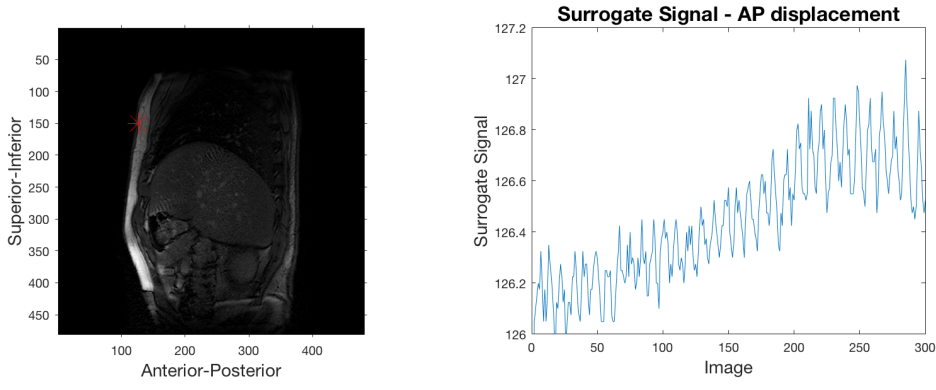
Three different respiratory parameters are derived from the measured surrogate data. These are the signal value, its gradient (temporal derivative) and the respiratory phase.

The temporal gradients are computed by calculating the difference in surrogate signal values between consecutive images. For example, \mathbf{I}_1 is assigned the difference in signal value between \mathbf{I}_1 and \mathbf{I}_2 . Note that this reduces the number of data points from 300 to 299 ($\mathbf{I}_1, \dots, \mathbf{I}_{299}$) when incorporating the temporal gradient into our correspondence model.

The respiratory phase is computed by finding the signal's local minima (troughs in Figure 8, where the gradient changes from a negative to a positive value) and maxima (peaks in Figure 8, where the gradient changes from a positive to a negative value). In general, the local minima represent end-exhalation points while the local maxima represent end-inhalation points (the skin surface reaches its maximum AP displacement when finishing to breath in). Note that this is not always the case; irregular breathing may produce additional local minima and maxima, not corresponding to end-inhalations/exhalations. In this study, these points have not been identified. However, we do identify sequences of images where there does not appear to be a minima (end-exhalation) between two maximas (end-inhalation). An example of this occurs between \mathbf{I}_{229} and \mathbf{I}_{238} , where a minima has been manually introduced at \mathbf{I}_{234} during preprocessing. This may occur due to 'breath-skipping' or in fact, to irregular breathing (where the subject has taken a very short exhalation between inhalations).

End-exhalation points are given a phase value of 0%. The phase value for end-inhalation points is assigned by calculating their average position in between end-exhalations. This corresponds to a phase value of 51.73%. This procedure preserves a roughly even phase distribution over the entire fraction, even if the subject spends slightly more time inhaling than exhaling. For each image not corresponding to end-inhalation/exhalation, the phase value is computed via linear interpolation between the end-inhalation and end-exhalation phase values. Note that phase estimations (and maxima/minima location) are coarse given the temporal resolution of the images. Faster image acquisition times would provide more accurate estimations.

Using multiple physical signals. A secondary physical signal has been generated for use in some correspondence models. Again, it corresponds to AP skin surface displacement but in a different part of the subject's upper body. The secondart surrogate signal is generated by finding the AP location of the skin surface at SI= 150 pixels in each of the images. Again, such location is estimated by locating the first point in the image with an intensity of 70 when coming from the anterior side. Figure 9 highlights the location of the skin surface at SI= 150 pixels with a red asterisk. Figure 10 shows a plot of the secondary surrogate signal over each image.



Figures 9 and 10 (left to right). Figure 7: 2D sagittal MR image highlighting the location of the skin surface at SI= 150 pixels. Figure 8: Plot of the **secondary** physical surrogate signal (AP displacement) over each image.

The secondary surrogate signal is of poorer quality than the first, showing a systematic increase throughout the fraction, most probably not due to motion of the internal anatomy (this has its consequences - overfitting). However, it provides an anatomic surrogate inside the thorax, in contrast to the abdominal surrogate provided by the primary signal. Whereas, the most commonly used anatomic surrogate is the AP motion of the abdominal surface [15-17], intuition suggests that thoracic surrogates should correlate better with respiratory motion. Surrogates in the diaphragm [18] and the carina [19] have correlated well with lung tumor motion in previous studies. In this case, the secondary physical signal corresponds to the AP displacement of the chest.

2.2.3 Choice of correspondence model

The following correspondence models are investigated to relate the motion of the internal anatomy (B-spline registration results) to the respiratory parameters outlined in **2.2.2. Appendix A** provides a comprehensive list of all the correspondence models utilised in this study.

Linear model

A linear correspondence model relates the motion estimates \mathbf{M}_{F_t} to a linear combination of surrogate signals via,

$$\mathbf{M}_{F_t} = \mathbf{C}\mathbf{S}_t + \mathbf{C}_0, \quad (2)$$

where $\mathbf{S}_t = [s_{t,1}, \dots, s_{t,N_s}]$ is a vector of surrogate signals (there are N_s of these), \mathbf{C} is a coefficient matrix of size $N_m \times N_s$ and \mathbf{C}_0 is a vector of N_m constants.

One surrogate signal ($N_s = 1$): These are the most common models in the literature [18, 20-23], corresponding to a simple linear correlation between the primary surrogate signal and the respiratory motion. The surrogate signal is simply the value of the primary surrogate data; in our experiment, it constitutes the AP displacement of the subject’s abdominal skin surface. With a single signal, it is not possible to differentiate between inhalation and exhalation i.e. intra-cycle variation cannot be modelled. Respiratory motion is limited to following identical trajectories (following a straight line) during each breath [5]. In addition, only a very small level of inter-cycle variation can be represented; depending on the depth of each breath, the motion can take different distances along its established breath to breath trajectory [5]. Although, a linear model may not be too realistic, it can provide sufficient accuracy over short time frames in some clinical scenarios e.g. the Cyberknife system [24,25]. However, it is not appropriate when there is considerable hysteresis since it does not capture the necessary variation.

Two or more surrogate signals ($N_s \geq 2$): To model both intra-cycle variation and more complex inter-cycle variation, more than one surrogate signal is required. One can use a derived secondary signal e.g. the gradient (temporal derivative) of the physical signal, alongside the original signal value, as proposed in [26]. One can also incorporate both physical signals into the correspondence model, as suggested in [27,28]. Using both the primary physical signal (abdomen displacement) and the secondary physical signal (chest displacement) allows modelling variations between thoracic and abdominal breathing [35].

Utilising multiple surrogate signals gives also more flexibility to the correspondence model, potentially allowing it to model more complex motion e.g. hysteresis, inter-cycle variation. However, more surrogate signals make the model more prone to overfitting, specially when the signals are correlated with each other [29,30], and expose the model to the “curse of dimensionality”. More signals and degrees of freedom require more data to fit the correspondence model, inducing a greater risk of over-fitting.

Separating inhalations and exhalations. We have broken down the data into inhalation and exhalation data and built separate correspondence models for each (as proposed in [12]). Surrogate signals with negative gradients are regarded as exhalation data whereas positive gradients are associated with inhalations. This modification allows for the modelling of intra-cycle variation. Now respiratory motion may follow different paths between inhalation and exhalation. Inter-cycle variation can be modelled given different lengths can be moved along trajectories for each breath.

Polynomial model

We utilise polynomial correspondence models [12] relating the motion estimates \mathbf{M}_{F_t} to a surrogate signal $s_{t,1}$ via,

$$\mathbf{M}_{F_t} = \sum_{i=0}^p \mathbf{C}_i s_{t,1}^i \quad (3)$$

or to two surrogate signals $s_{t,1}$ and $s_{t,2}$, via:

$$\mathbf{M}_{F_t} = \sum_{i=0}^p \sum_{j=0}^{n-i} \mathbf{C}_{i,j} s_{t,1}^i s_{t,2}^j, \quad (4)$$

where p is the polynomial order and \mathbf{C}_i , $\mathbf{C}_{i,j}$ are polynomial coefficient vectors. We explore similar techniques than those outlined for the linear model for polynomial models of the second (quadratic) and third (cubic) order. Polynomial models of higher order are not explored as they are more prone to overfitting. Again, with a single signal, respiratory motion is limited to following the same trajectory during inhalation and exhalation (which can now take the form of a curve), and is not appropriate when there is considerable hysteresis. As for the linear model, building separate polynomial models for inhalations and exhalations help resolve this problem.

Fourier Series model

Utilising the respiratory phase as a surrogate signal assumes periodic breathing. In addition, it allows the modelling of intra-cycle variation, constraining respiratory motion to follow an identical “loop” during each cycle (no inter-cycle variation can be modelled). Even though we have explored incorporating the respiratory phase alongside the primary physical signal into linear and polynomial correspondence models (as per [38]), these do not fully exploit its periodicity. For this reason, the following Fourier series model is proposed (as suggested in [39]):

$$\mathbf{M}_{F_t} = \alpha_0 + \sum_{i=1}^n (2\pi i \theta + \omega_i), \quad (5)$$

Here θ is the respiratory phase (the position of the signal in the respiratory cycle). Function (5) is by definition periodic, ensuring a smooth transition between respiratory cycles. The function is defined by the amplitudes $\alpha_1, \dots, \alpha_n$ and the phase offsets $\omega_1, \dots, \omega_n$ of its n harmonic frequencies (α_0 is the zero-frequency offset). In this study, we explore fitting the respiratory motion to the respiratory phase with first, second, third and fourth order Fourier functions. The ‘order’ is defined as the number of frequencies used in the series i.e. a first order Fourier function has three coefficients and increasing the order by one requires two extra coefficients.

A key to all 18 models implemented is provided in **Appendix A**. Numerical results are provided for all of the models. Graphs/plots are provided for selected models. The Table of Results is in **Appendix B**.

2.2.4 Choice of model-fitting procedure

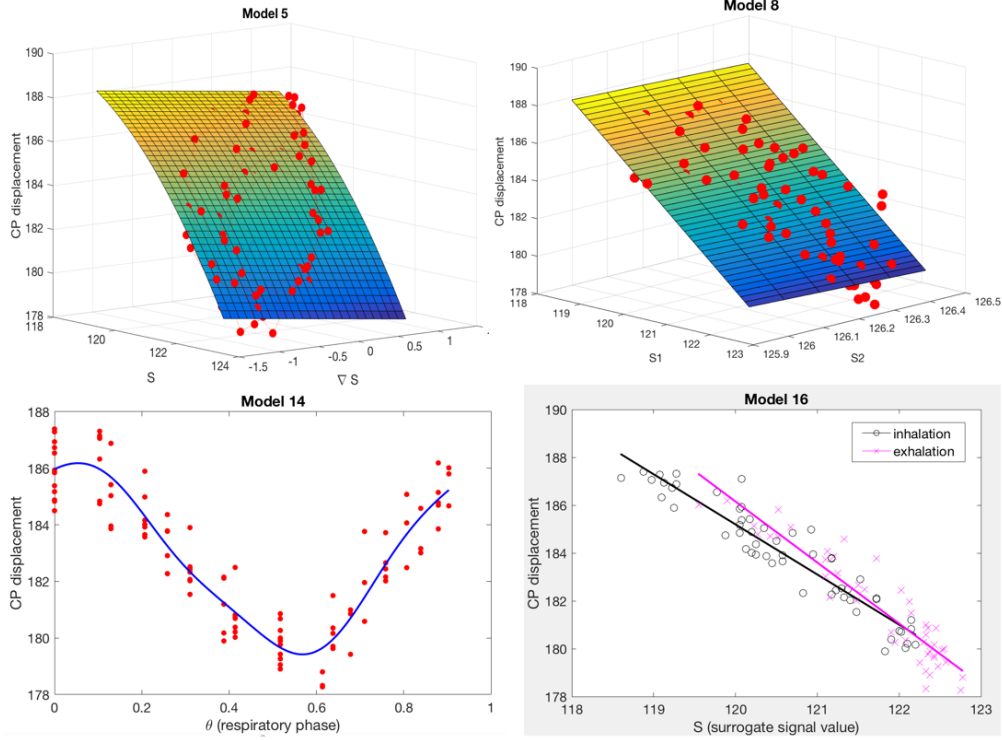
Linear least squares has been used to fit all linear/polynomial models e.g. in equation (3), the model parameters are found from training data via finding argmin $(\mathbf{M}_{F_t} - \sum_{i=0}^p \mathbf{C}_i s_{t,1}^i)^2$. For this purpose we use the MATLAB function `mldivide`. Notice that even though the data is not i.i.d, we are effectively treating it as such. The MATLAB function `fit` is used to fit Fourier series models.

3 Methods and results

3.1 Fitting the correspondence models

The first 100 registration results are used for fitting the models (the other 200 are used for assessing the results). To eyeball the data, the SI displacement of control point (CP) 30,20 is plotted for the first 100 registration results. All models are fit to this displacement. Figures 11 to 14 show plots of model fit over plots of this CP displacement for Model 5, Model 8, Model 14 and Model 16. Once the fits have been visualised, a separate

model is fit to every CP displacement. This is done by forming a large matrix containing all 100 registration results for every CP displacement (AP direction), and fitting all the models simultaneously. The mean residual sum of squared errors, its standard deviation and its 95th and 99th percentiles are computed over all AP and SI displacements for all models fitted (see Table of Results).



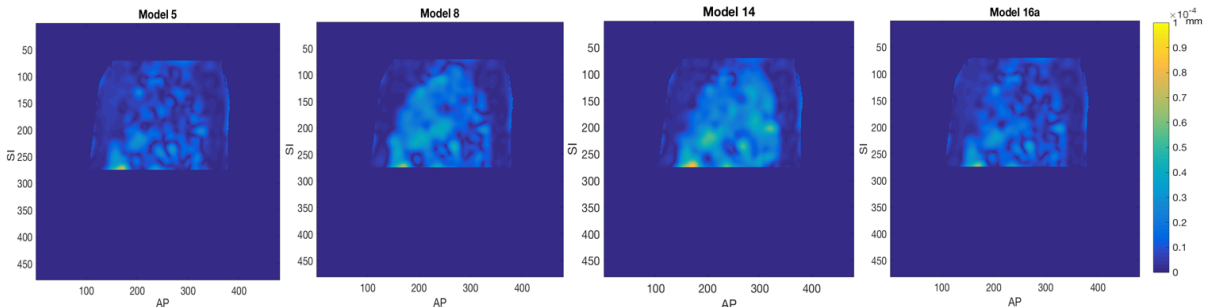
Figures 11-14: Plots of fit over the (SI) displacement of CP 30,20 for Model 5, Model 8, Model 14 and Model 16. ∇S is the gradient of the primary physical signal. For M8, S_1 is the primary physical signal, S_2 the secondary.

3.2 Evaluating the correspondence models

The remaining 200 registration results are used as test images to evaluate the motion models. Each model is utilised to estimate the transformation (CP displacements) for the surrogate signal value corresponding to the target test image. The model estimates are assessed using the following three techniques: visual assessment, computing the deformation field error and computing the landmark error.

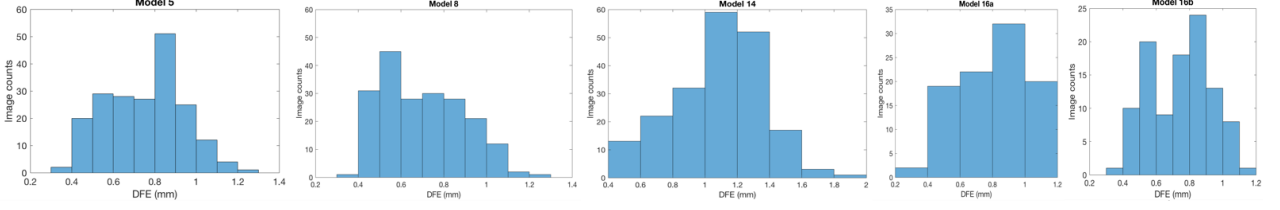
Visual assessment: Initially, the transformations estimated by the models are utilised to deform the test images. Upon displaying the deformed images (as in Figure 4), we observe residual motion below the diaphragm (particularly in the anterior-inferior organs of the lower digestive system) for all models. On the other hand, there is no considerable residual motion above the diaphragm. No residual motion would be observed in the deformed images given perfect motion estimation. Therefore, most of our models work reasonably well, producing less residual motion than the registrations in both thorax and abdomen (in any case, pixels outside the deformation field mask (most of the abdomen) should be ignored; not being indicative of the model's performance).

Deformation field error (DFE): The DFE is the difference between the deformation field resulting from the predicted CP displacements and the (true) deformation field produced by the registration results for the target image. The ℓ^2 norm of the DFE is computed at each pixel (ignoring those outside the field mask area) for all images. Summary statistics (mean, standard deviation, 95th and 99th percentiles) are provided for all models in the Table of Results. Figures 15 to 18 show heat maps visualising the DFE for I_{125} (test image 25) produced by models 5, 8, 14 and 16a (since the image in question corresponds to an inhalation - positive physical surrogate signal gradient). Notice the units have been converted from pixels to mm.



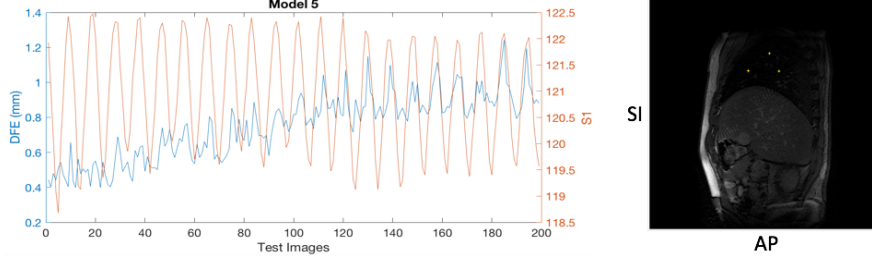
Figures 15-18 (left to right): DFE (in mm) heatmap for I_{125} for Model 5, Model 8, Model 14 and Model 16a.

Also notice that for the inhalation models (16a, 17a, 18a), I_5 has been used as the reference image (the subject is inhaling) instead of I_6 (which corresponds to exhalation). Figures 19-23 present histograms of the mean DFE distribution for the aforementioned models and Model 16b.



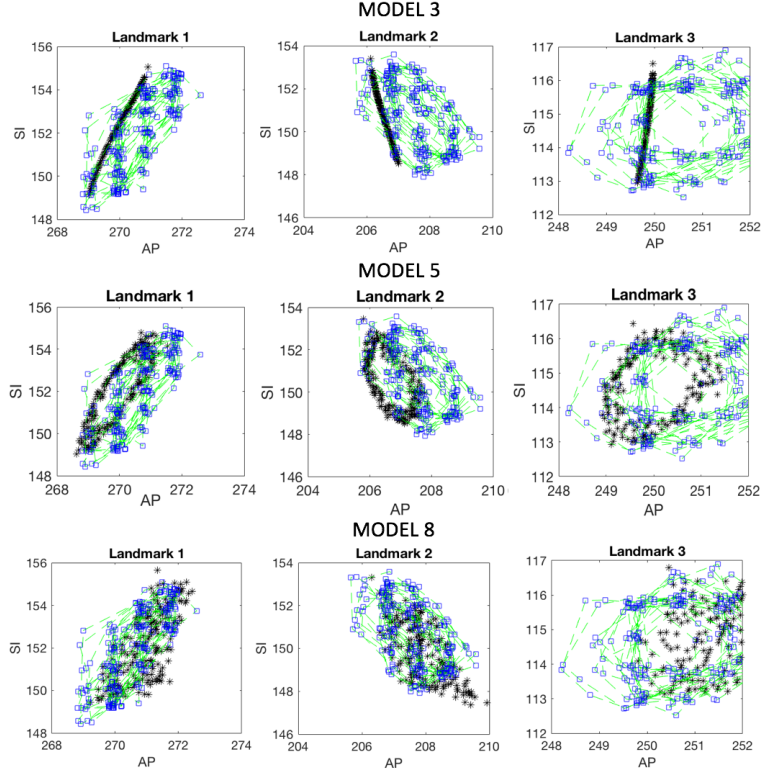
Figures 19-23 (left to right): Histogram counts displaying mean DFE distributions for models 5, 8, 14, 16a, 16b.

Figure 24 present the mean DFE over the test images against surrogate signal values for Model 5 (primary physical signal plotted). We can observe the correlation between the DFE and the respiratory motion. Notice how the DFE increases during inhalation; the reference target image I_6 corresponds to end-exhalation.



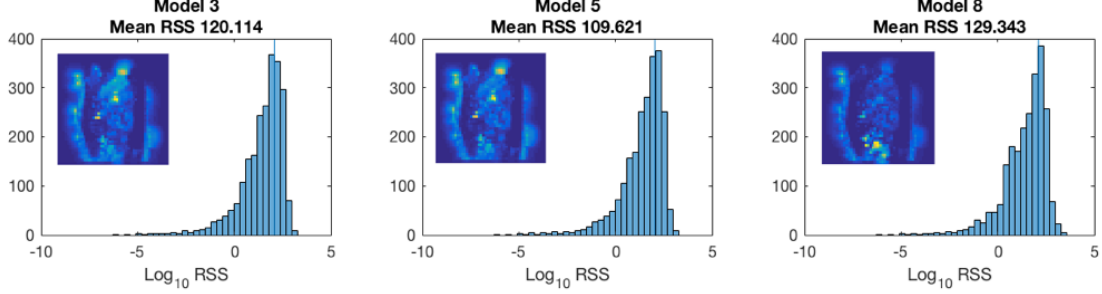
Figures 24, 25. Figure 24: DFE (mm) plotted against physical surrogate signal value over the test images for Model 5. Figure 25: The location of the three anatomical landmarks.

Landmark error: The landmark error is defined as the difference between the anatomical landmark locations estimated by our models and those locations provided. Figure 25 displays the location of the provided landmarks in the subject's chest. The location estimations are performed by transforming the landmark locations from the reference image (I_6 , except in the case of the inhalation models) into each test image's space (using the transform estimated by each model). The landmark error is computed for each landmark/test image for all models. Summary statistics (mean, standard deviation, 95th and 99th percentiles) are provided for selected models (see Table of Results) for both the AP and SI components and for the ℓ^2 norm of the landmark errors. Figures 26-34 present landmark registration plots over all test images for models 3, 5 and 8.

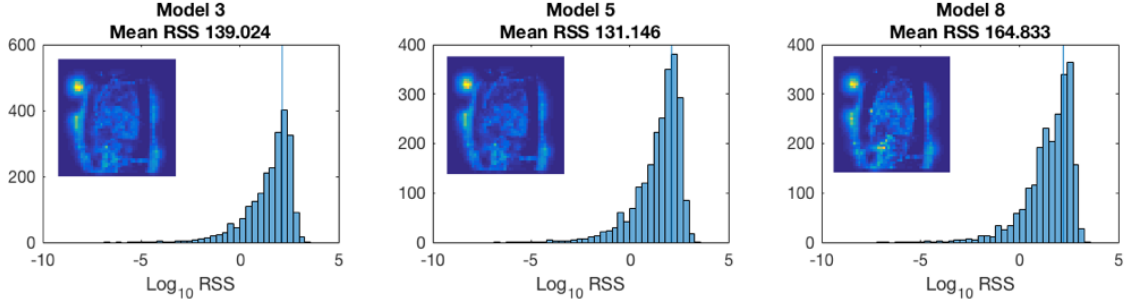


Figures 26-34. Landmark registration results for Model 3, Model 5 and Model 8. The blue squares represent the landmark ground truth locations (joined sequentially by the green lines). The black crosses represent the landmark locations estimated by each model.

Model selection: The Akaike Information Criterion (AIC) and Bayesian Information Criterion are computed for selected models in both AP and SI directions (see Table of Results). The AIC is given by $AIC = 2N - 2\log L$, and the BIC is given by $BIC = N\log K - 2\log L$. Here, N is the number of model parameters, K is the number of test points and L is the maximised value of the likelihood function for the model (in this case $L = RSS/K$ where RSS is the residual sum of square errors in a specific direction for the model fit). Figures 35-37 present histograms visualising the RSS distribution in the AP direction for Model 3, Model 5 and Model 8. Figures 38-40 visualise the RSS distribution in the SI direction for the aforementioned models. Heat maps visualising the RSS error intensity for each image pixel are enclosed. When comparing results, note that there twice the number of test data points than training data points.

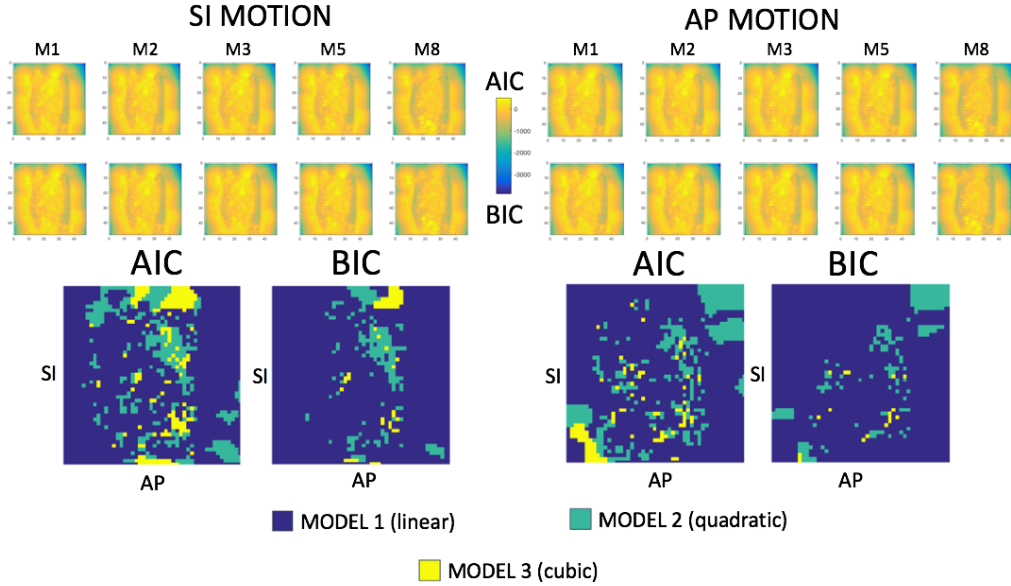


Figures 35-37: Histograms of RSS distribution in the AP direction for Model 3, Model 5 and Model 8.



Figures 38-40: Histograms of RSS distribution in the SI direction for Model 3, Model 5 and Model 8.

The AIC and BIC for AP/SI motion have been evaluated per pixel. The means over all pixels are reported in the Table of Results. Figures 41-60 present information criteria heatmaps (mean AIC/BIC per pixel) for motion in both directions for models 1,2,3,5 and 8. Figures 61-64 visualise the ‘best-performing’ model (that giving the lowest AIC/BIC) per pixel among models 1-3.



Figures 41-64 (left to right, then top to bottom): Figures 41-45: AIC heatmaps for SI motion. Figures 46-50: AIC heatmaps for AP motion. Figures 51-55: BIC heatmaps for SI motion. Figures 56-60: BIC heatmaps for AP motion. Figures 61-64: Visualisation of models with lowest information criteria for models 1, 2 and 3.

3.3 Model uncertainty estimation

Both classical and wild bootstrapping are used to estimate the distribution of model parameters and their uncertainty for models 1 and 3. Figure 65 shows classical bootstrap estimation maps of the model parameters. Figure 66 presents distributions of the parameters for CP 30,20 using classical (left) and wild (right) bootstrap (models 1-3). 500 repetitions have been carried out.

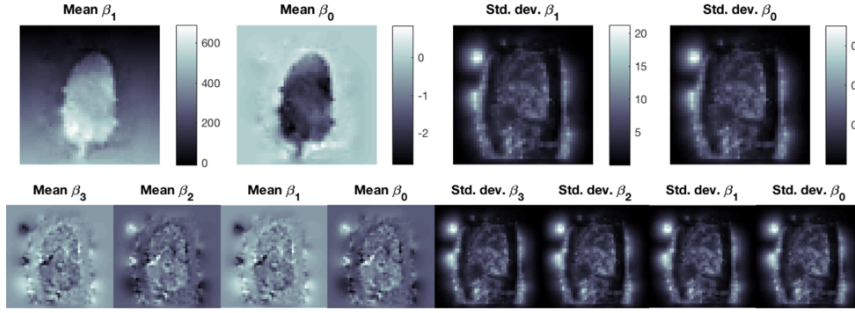


Figure 65: Classical bootstrap maps for the parameters of models 1 and 3 (β_0, β_1 for model 1 - linear).

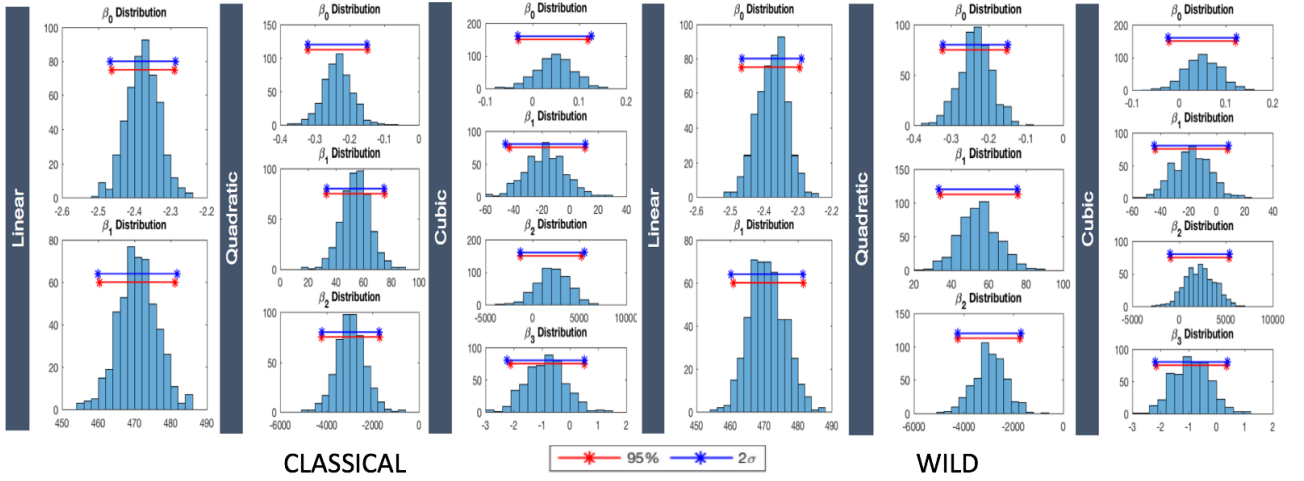


Figure 66: Parameter distributions with confidence intervals for models 1-3 using classical and wild bootstrap.

4 Discussion

Upon examination of the figures and the Table of Results (Appendix B), there are no significant differences in performance between models 1-3 (linear, quadratic and cubic models with one physical surrogate signal). These models, despite their simplicity, fit the training data reasonably well. They give greater RSS errors, however, than other models with the same numbers of parameters. For example, models 4 and 8 give better training fits (lower RSS) than model 2 (all with 3 parameters). The apparent superiority of models 8-11 (two physical surrogate signals) breaks down when fitting these to the test data (as seen in the test RSS distributions in figures 37 and 40). As mentioned in Section 2, the poorer quality of the secondary physical signal (showing a systematic increase over time), leads to overfitting on the training set. Models 8-11 have lower training RSS but greater test RSS than their one-signal counterparts (they are capturing an underlying pattern which does not correspond to the respiratory motion of the internal anatomy). Our Fourier series models appear to be a lost cause, with the largest error values across the board. This is perhaps due to poor preprocessing before model fitting.

We can observe the limitations on the type of motion modelled by some of our models in Figures 26-34. Firstly, it becomes apparent that models with one physical surrogate signal are constrained to following identical trajectories along a straight line/curve during each breath (Figures 26-28). It is not possible to differentiate between inhalation and exhalation i.e. intra-cycle variation cannot be modelled. In addition, only a very small level of inter-cycle variation can be represented. Depending on the depth of each breath, the motion can take different distances along the straight line/curve. As seen in Figures 29-31 (gradient) and Figures 32-34 (secondary physical signal), introducing another signal allows the modelling of more complex variation. Using both a signal abdomen displacement and another for chest displacement perhaps allows modelling variations between thoracic and abdominal breathing. Observe how introducing the gradient to a polynomial model (Figures 29-31) allows us the model to follow different trajectories during inhalation/exhalation. Now, respiratory motion is constrained to follow a fixed loop during each cycle. Unlike for models 8-11, it appears no inter-cycle variation can be modelled.

Each method of evaluating the models has its advantages and disadvantages. Visual assessment has the advantage of simplicity: it is easy to give a rough assessment of model performance and to spot errors in a procedure. On the other hand, it is too simple to provide a systematic framework for model comparison. Evaluating the deformation error provides a more quantitative approach and more dense information than a simple control point error. However, its values are hard to interpret and (incorrectly) assume that deformation registrations are perfect. Using the landmark error has the advantage of interpretability and of being independent of the data at hand. Additionally, this evaluation method is able to connect model errors to underlying respiratory motion, providing a clearer interface with the matter of interest. Landmark error assessment is, however, difficult to implement in practice, since it requires the clinician to label landmarks on images. Alternatively, these labels could be acquired from template tracking.

The results of the different evaluation methods are generally in agreement. For example, correspondence models including a gradient, secondary physical signal or broken down into inhalation/exhalation tend to give both lower landmark and deformation field errors. Rarely does a model with a comparative low landmark error give a high DFE and viceversa. Results are within our expectations, giving models incorporating the signal gradient the lowest landmark errors, and giving models with a secondary physical signal the lowest DFEs. Models broken down into inhalation/exhalation always outperform their counterparts with lower landmark and deformation field errors. I think the current 100/200 data split is reasonable given the small size of the entire dataset (300 images). However, the small size of the training set leads to overfitting in some scenarios (models 8-11), with some models not generalising well to a larger dataset. Possible different approaches to be used include computing the deformations at each pixel; this has the disadvantage of being very expensive computationally. Alternatively, one could also find the error in the control points (this is a similar approach to the current one) or use other fitting methods e.g. Tikhonov regularisation, PCA.

The ‘best’ model (from 1,2,3,5,8) according to the mean SI AIC is Model 5. According to the mean SI BIC, its Model 1, and according to both AP measures it is Model 8. This is somewhat in agreement with our previous assessment results. Models 5 and 8 still give good performance but have been penalised for having 1/2 more parameters than 1. Strangely, Model 8 gives the ‘best’ performance (lowest AIC/BIC) in the AP direction but by far the worst in the SI direction. It appears the SI direction is that triggering its overfitting. Figures 61-64 suggest that given only one (physical) surrogate signal, some parts of the motion are better described by the more complex (quadratic, cubic) models. We use both classical and wild bootstrap methods to explore this. Wild bootstrapping assumes that the model is correct and on top of that has a Gaussian noise model. If the model is ‘incorrect’, we will observe systematic non-Gaussianity in the errors. This is observed in the linear/quadratic plots in Figure 66. The skewing in the lower order models suggests that the cubic model is doing a better job (at least for CP 30,20). Potential future work is discussed in Appendix C.

Appendix A: Models

Key of implemented models

The following correspondence models have been implemented in this study:

Model 1: Linear relationship between respiratory motion and the primary (abdominal) physical surrogate signal.

Model 2: Quadratic (second order polynomial) relationship between respiratory motion and the primary physical surrogate signal.

Model 3: Cubic (third order polynomial) relationship between respiratory motion and the primary physical surrogate signal.

Model 4: Linear relationship between respiratory motion and the primary physical surrogate signal. Linear relationship between respiratory motion and the derived gradient of the surrogate signal.

Model 5: Quadratic relationship between respiratory motion and the primary physical surrogate signal. Linear relationship between respiratory motion and the gradient of the surrogate signal.

Model 6: Quadratic relationship between respiratory motion and the primary physical surrogate signal. Quadratic relationship between respiratory motion and the gradient of the surrogate signal.

Model 7: Cubic relationship between respiratory motion and the primary physical surrogate signal. Quadratic relationship between respiratory motion and the gradient of the surrogate signal.

Model 8: Linear relationship between respiratory motion and a primary (abdominal) physical surrogate signal. Linear relationship between respiratory motion and a secondary (thoracic) physical surrogate signal.

Model 9: Linear relationship between respiratory motion and the primary physical surrogate signal. Linear relationship between respiratory motion and the gradient of the primary surrogate signal. Linear relationship between respiratory motion and the secondary physical surrogate signal.

Model 10: Linear relationship between respiratory motion and the primary physical surrogate signal. Linear relationship between respiratory motion and the gradient of the primary surrogate signal. Linear relationship between respiratory motion and the secondary physical surrogate signal. Linear relationship between respiratory motion and the gradient of the secondary surrogate signal.

Model 11: Quadratic relationship between respiratory motion and the primary physical surrogate signal. Linear relationship between respiratory motion and the gradient of the primary surrogate signal. Quadratic relationship between respiratory motion and the secondary physical surrogate signal. Linear relationship between respiratory motion and the gradient of the secondary surrogate signal.

Model 12: First order Fourier series relating respiratory motion to the respiratory phase.

Model 13: Second order Fourier series relating respiratory motion to the respiratory phase.

Model 14: Third order Fourier series relating respiratory motion to the respiratory phase.

Model 15: Fourth order Fourier series relating respiratory motion to the respiratory phase.

Model 16: Linear relationship between respiratory motion and the primary (abdominal) physical surrogate signal. **Separate models built for exhalation (16b) and inhalation (16a) data.**

Model 17: Quadratic (second order polynomial) relationship between respiratory motion and the primary physical surrogate signal. **Separate models built for exhalation (17b) and inhalation (17a) data.**

Model 18: Cubic (third order polynomial) relationship between respiratory motion and the primary physical surrogate signal. **Separate models built for exhalation (18b) and inhalation (18a) data.**

Appendix B: Table of Results

Summary statistics are provided in the form (mean \pm standard deviation/95th percentile/99th percentile). 16a means 16 (inhalation); 16b means 16 (exhalation) etc. Bare in mind there are lesser numbers of training/test data points when splitting the data. This explains the much lower RSS values for these models.

Model	SI RSS error for training fit	AP RSS error for training fit	Deformation Field Error (mm)
1	56.1 ± 90.5/213.5/430.5	42.7 ± 63.2/160.9/298.9	0.83 ± 0.23/1.23/1.30
2	54.5 ± 89.0/208.9/421.9	41.6 ± 61.5/158.3/291.2	0.83 ± 0.23/1.24/1.29
3	53.8 ± 87.9/205.9/421.3	41.1 ± 60.8/156.6/290.8	0.83 ± 0.23/1.24/1.29
4	53.2 ± 89.0/208.6/427.0	38.9 ± 60.7/156.3/296.8	0.76 ± 0.18/1.04/1.17
5	51.5 ± 87.5/202.5/419.2	37.9 ± 59.0/153.0/286.9	0.75 ± 0.19/1.04/1.17
6	50.7 ± 86.5/199.7/411.0	37.3 ± 58.3/150.9/282.0	0.75 ± 0.19/1.03/1.16
7	50.0 ± 85.5/196.4/407.3	36.8 ± 57.6/147.2/280.7	0.75 ± 0.19/1.02/1.16
8	53.8 ± 88.7/208.6/424.3	39.6 ± 60.0/154.1/288.9	0.70 ± 0.19/1.03/1.13
9	51.2 ± 87.5/202.7/423.2	37.0 ± 58.6/150.4/285.0	0.66 ± 0.15/0.92/0.97
10	50.0 ± 85.8/201.6/420.7	36.3 ± 57.8/147.7/278.6	0.70 ± 0.18/0.99/1.02
11	47.8 ± 82.9/192.6/415.0	34.8 ± 55.3/143.5/257.9	0.78 ± 0.29/1.35/1.56
12	60.6 ± 92.8/226.6/434.5	39.4 ± 59.5/157.2/284.2	0.78 ± 0.20/1.07/1.14
13	58.9 ± 90.4/220.2/419.5	38.0 ± 57.7/151.0/274.5	0.78 ± 0.20/1.07/1.14
14	57.6 ± 88.7/215.9/408.2	36.9 ± 55.8/146.0/264.3	0.78 ± 0.20/1.06/1.16
15	56.4 ± 86.9/212.0/398.7	36.0 ± 54.2/140.7/257.9	0.78 ± 0.20/1.08/1.17
16a	29.0 ± 48.0/115.6/218.8	21.5 ± 32.9/85.7/157.3	0.75 ± 0.18/1.04/1.11
16b	23.0 ± 40.8/92.3/212.9	17.1 ± 27.3/67.9/135.0	0.79 ± 0.20/1.06/1.14
17a	28.2 ± 47.3/112.6/217.3	20.9 ± 31.7/84.1/153.9	0.75 ± 0.19/1.05/1.12
17b	21.8 ± 38.9/88.1/189.5	16.5 ± 26.7/66.4/130.4	0.76 ± 0.19/1.03/1.12
18a	27.5 ± 45.9/110.4/216.4	20.4 ± 31.0/82.5/150.6	0.76 ± 0.19/1.07/1.12
18b	21.3 ± 38.1/86.0/188.3	16.1 ± 26.1/65.0/130.2	0.76 ± 0.19/1.00/1.09
Model	SI Landmark 1 (L1) error	AP L1 error	ℓ^2 norm of L1 error
1	0.51 ± 0.35/1.10/1.46	0.84 ± 0.57/1.78/2.18	1.05 ± 0.56/1.99/2.43
2	0.49 ± 0.31/1.08/1.26	0.84 ± 0.56/1.75/2.15	1.04 ± 0.52/1.91/2.33
3	0.50 ± 0.31/1.07/1.24	0.83 ± 0.56/1.76/2.17	1.04 ± 0.52/1.92/2.32
5	0.33 ± 0.23/0.82/0.93	0.65 ± 0.36/1.23/1.44	0.79 ± 0.32/1.30/1.55
8	0.50 ± 0.33/1.09/1.22	0.56 ± 0.41/1.33/1.66	0.82 ± 0.41/1.61/1.86
14	1.53 ± 0.87/3.28/3.62	0.98 ± 0.71/2.12/2.26	1.91 ± 0.94/3.57/4.27
16a	0.38 ± 0.26/0.85/1.15	0.72 ± 0.46/1.58/1.81	0.86 ± 0.45/1.71/1.93
16b	0.49 ± 0.29/1.01/1.13	0.69 ± 0.38/1.33/1.56	0.90 ± 0.36/1.58/1.83
Model	SI Landmark 2 (L2) error	AP L2 error	ℓ^2 norm of L2 error
1	0.39 ± 0.30/0.93/1.45	1.06 ± 0.71/2.18/2.73	1.22 ± 0.61/2.20/2.75
2	0.39 ± 0.29/0.92/1.41	1.06 ± 0.71/2.21/2.75	1.21 ± 0.62/2.24/2.78
3	0.39 ± 0.30/0.92/1.43	1.06 ± 0.71/2.21/2.75	1.22 ± 0.63/2.24/2.78
5	0.33 ± 0.28/0.90/1.25	0.88 ± 0.42/1.52/1.90	1.00 ± 0.38/1.55/1.91
8	0.86 ± 0.49/1.81/2.00	0.59 ± 0.40/1.33/1.62	1.10 ± 0.53/2.07/2.46
14	1.08 ± 0.72/2.43/3.13	0.94 ± 0.58/1.86/2.45	1.59 ± 0.62/2.63/3.17
16a	0.38 ± 0.33/1.09/1.44	0.86 ± 0.49/1.63/2.08	1.02 ± 0.43/1.64/2.08
16b	0.30 ± 0.24/0.68/1.00	0.97 ± 0.55/1.88/2.30	1.07 ± 0.49/1.88/2.30
Model	SI Landmark 3 (L3) error	AP L3 error	(ℓ^2 norm) of L3 error
1	0.33 ± 0.22/0.79/1.04	1.06 ± 0.85/2.67/2.78	1.16 ± 0.80/2.71/2.83
2	0.31 ± 0.21/0.73/0.95	1.06 ± 0.84/2.64/2.75	1.16 ± 0.79/2.69/2.81
3	0.31 ± 0.21/0.73/0.95	1.06 ± 0.84/2.64/2.75	1.16 ± 0.79/2.69/2.81
5	0.27 ± 0.21/0.69/0.85	0.77 ± 0.44/1.53/1.97	0.86 ± 0.41/1.58/1.97
8	0.31 ± 0.21/0.70/0.98	1.02 ± 0.68/2.28/2.72	1.11 ± 0.63/2.32/2.75
14	0.93 ± 0.57/2.10/2.36	0.99 ± 0.76/2.30/2.59	1.50 ± 0.70/2.64/3.00
16a	0.33 ± 0.23/0.74/0.90	0.77 ± 0.55/1.93/2.11	0.90 ± 0.50/1.94/2.22
16b	0.27 ± 0.19/0.58/0.89	0.93 ± 0.60/2.02/2.22	1.00 ± 0.57/2.02/2.23
Model	Number of parameters	SI/AP Mean AIC (whole image)	SI/AP Mean BIC (whole image)
1	2	-385.2/-391.2	-378.6/-384.6
2	3	-382.6/-387.9	-327.7/-378.0
3	4	-378.7/-384.7	-365.5/-371.5
5	4	-387.4/-394.8	-374.2/-381.7
8	3	-371.9/-395.5	-362.0/-385.6

Appendix C: Future work

There is scope to incorporate the following techniques. Unfortunately, these could not be implemented for this study due to time constraints.

Surrogate data

- Using a time delayed value of the surrogate signal (a precursor) as a derived signal [29]. This idea can perhaps be extended to multiple precursors i.e. multiple time-lagged signals with a different length delay for each [31].
- Using an estimate of signal amplitude (the difference between the values at end-inhalation and end-exhalation) as a derived surrogate signal. [32]
- Utilising different secondary physical signals or using more than two physical signals e.g. AP displacement of the diaphragm or carina instead of (or alongside) chest displacement.
- Exploring more combinations of multiple physical and derived signals [13, 36]. In addition, using a binary signal to differentiate inhalation from exhalation instead of building separate models for each [37].
- **More data.**

Correspondence Model

- Using a piece-wise linear model to relate respiratory motion to either a physical surrogate signal [33] or to the respiratory phase [34]. The first option cannot model hysteresis but can model some inter-cycle variation. On the other hand, the second option cannot model inter-cycle variation but can model hysteresis.
- Utilising B-spline correspondence models to relate respiratory phase and respiratory motion [38].
- Implementing other correspondence models proposed in the literature e.g. neural networks, fuzzy logic and support vector regression.

Model-fitting procedure

- Using Principal Component Analysis (PCA) to fit the correspondence model. This would reduce the dimensionality of the problem and possibly alleviate the “curse of dimensionality” for some of the implemented models (reducing the available degrees of freedom).
- Implementing other fitting techniques proposed in the literature e.g. There have been a number of other fitting methods proposed in the literature e.g canonical correlation analysis, support vector regression, Nelder-Mead optimisation and the Levenberg-Marquardt algorithm.

References

- [1] Nehmeh, S.A., Erdi, Y.E., 2008. Respiratory motion in positron emission tomography/computed tomography: a review. *Seminars in Nuclear Medicine* 38, 167–176.
- [2] Scott, A.D., Keegan, J., Firmin, D.N., 2009. Motion in cardiovascular MR imaging. *Radiology* 250, 331–351.
- [3] Hawkes, D.J., Barratt, D., Blackall, J.M., Chan, C., Edwards, P.J., Rhode, K., Penney, G.P., McClelland, J., Hill, D.L.G., 2005. Tissue deformation and shape models in imageguided interventions: a discussion paper. *Medical Image Analysis* 9, 163–175.
- [4] Shirato, H., Shimizu, S., Kunieda, T., Kitamura, K., van Herk, M., Kagei, K., Nishioka, T., Hashimoto, S., Fujita, K., Aoyama, H., Tsuchiya, K., Kudo, K., Miyasaka, K., 2000. Physical aspects of a real-time tumor-tracking system for gated radiotherapy. *International Journal of Radiation Oncology Biology Physics* 48, 1187–1195.
- [5] McClelland, J.R., Hawkes, D.J., Schaeffter, T., King A.P., 2013. Respiratory motion models: A review. *Medical Image Analysis* 17, 19–42.
- [6] McClelland, J.R., 2013. Estimating internal respiratory motion from respiratory surrogate signals using correspondence models. In: *4D Modeling and Estimation of Respiratory Motion for Radiation Therapy* (pp. 17–32), Berlin, Springer.
- [7] Wilms, M., Werner, R., Ehrhardt, J., Schmidt-Richberg, A., Schlemmer, H-P. and Handels, H., 2014. Multivariate regression approaches for surrogate-based diffeomorphic estimation of respiratory motion in radiation therapy. *Phys. Med. Biol.* 59, 1147–1164.
- [8] McClelland, J.R., Hughes, S., Modat, M., Qureshi, A., Ahmad, S., Landau, D.B., Ourselin, S., Hawkes, D.J., 2011. Inter-fraction variations in respiratory motion models. *Phys. Med. Biol.* 56, 251–272.
- [9] McClelland, J.R. et al., 2017. A generalized framework unifying image registration and respiratory motion models and incorporating image reconstruction, for partial image data or full images. *Phys. Med. Biol.*, at press.

- [10] McClelland, J.R, Webb S., Binnie D.M. and Hawkes D.J., 2007. Tracking ‘differential organ motion’ with a ‘breathing’ multileaf collimator: magnitude of problem assessed using 4D CT data and a motion-compensation strategy. *Phys. Med. Biol.* 52, 4805–26.
- [11] Webb, S., 2008. Adapting IMRT delivery fraction-by-fraction to cater for variable intrafraction motion. *Phys. Med. Biol.* 53, 1–21.
- [12] Blackall, J.M., Ahmad, S., Miquel, M.E., McClelland, J.R., Landau, D.B., Hawkes, D.J., 2006. MRI-based measurements of respiratory motion variability and assessment of imaging strategies for radiotherapy planning. *Phys. Med. Biol.* 51, 4147–4169.
- [13] Gao, G., McClelland, J., Tarte, S., Blackall, J., Hawkes, D., 2008. Modelling the respiratory motion of the internal organs by using canonical correlation analysis and dynamic MRI. In: *The First International Workshop on Pulmonary Image Analysis held at MICCAI*.
- [14] Koch, N., Liu, H.H., Starkschall, G., Jacobson, M., Forster, K., Liao, Z., Komaki, R., Stevens, C.W., 2004. Evaluation of internal lung motion for respiratory-gated radiotherapy using MRI: Part I - correlating internal lung motion with skin fiducial motion. *Int. J. Radiation Oncology Biol. Phys.* 60, 1459–1472.
- [15] Jiang, S.B., 2006. Technical aspects of image-guided respiration-gated radiation therapy. *Med. Dosim.* 31, 141–51.
- [16] Kanoulas, E., Aslam, J. A., Sharp, G.C., Berbeco, R., I., Nishioka, S., Shirato, H., Jiang, S.B., 2007. Derivation of the tumor position from external respiratory surrogates with periodical updating of the internal/external correlation. *Phys Med Biol* 52, 5443–56.
- [17] Wu, H., Zhao, Q., Berbeco, R. I., Nishioka, S., Shirato, H., Jiang, S.B., 2008. Gating based on internal/external signals with dynamic correlation updates. *Phys Med Biol* 53, 7137–50.
- [18] Cervino, L.I. , Chao, A.K.Y., Sandhu, A., Jiang, S.B., 2009. The diaphragm as an anatomic surrogate for lung tumor motion. *Physics in Medicine and Biology* 54, 3529–3541.
- [19] van der Weide, L., van Sornsens de Koste, J.R., Lagerwaard, F.J., Vincent, A., van Triest, B., Slotman, B.J., Senan, S., 2008. Analysis of carina position as a surrogate marker for delivering phase-gated radiotherapy. *Int J Radiat Oncol Biol Phys* 71, 1111–7.
- [20] Ahn, S., Yi, B., Suh, Y., Kim, J., Lee, S., Shin, S., Choi, E., 2004. A feasibility study on the prediction of tumour location in the lung from skin motion. *The British Journal of Radiology* 77, 588–596.
- [21] Beddar, A.S., Kainz, K., Briere, T.M., Tsunashima, Y., Pan, T., Prado, K., Mohan, R., Gillin, M., Krishnan, S., 2007. Correlation between internal fiducial tumor motion and external marker motion for liver tumors imaged with 4D-CT. *Int. J. Radiation Oncology Biol. Phys.* 67, 630– 638.
- [22] Cervino, L.I., Jiang, Y., Sandhu, A., Jiang, S.B., 2010. Tumor motion prediction with the diaphragm as a surrogate: a feasibility study. *Physics in Medicine and Biology* 55, 221–229.
- [23] Chi, P.C.M., Balter, P., Luo, D., Mohan, R., Pan, T., 2006. Relation of external surface to internal tumor motion studied with cine CT. *Medical Physics* 33, 3116–3123.
- [24] Hoogeman, M., Briac Prevost, J., Nuytens, J., Levendag, J.P.P., Heijmen, B., 2009. Clinical accuracy of the respiratory tumor tracking system of the cyberknife: assessment by analysis of log files. *Int. J. Radiation Oncology Biol. Phys.* 74, 297–303.
- [25] Seppenwoolde, Y., Berbeco, R.I., Nishioka, S., Shirato, H., Heijmen, B., 2007. Accuracy of tumour motion compensation algorithm from a robotic respiratory tracking system: A simulation study. *Medical Physics* 34, 2774–2784.
- [26] Low, D.A., Parikh, P., Lu, W., Dempsey, J., Wahab, S., Hubenschmidt, J., Nystrom, M., 2005. Novel breathing motion model for radiotherapy. *International Journal of Radiation Oncology Biology Physics* 63, 921–929.
- [27] Manke, D., Nehrke, K., Bornert, P., 2003. Novel prospective respiratory motion correction approach for free-breathing coronary MR angiography using a patient-adapted affine motion model. *Magnetic Resonance in Medicine* 50, 122–131.
- [28] Klinder, T., Lorenz, C., 2012. Respiratory motion compensation for image-guided bronchoscopy using a general motion model. In: *Proceedings of International Symposium on Biomedical Imaging (ISBI)*.
- [29] Klinder, T., Lorenz, C., Ostermann, J., 2009. Free-breathing intra and intersubject respiratory motion capturing, modeling, and prediction. In: *Proceedings of SPIE Medical Imaging: Image Processing*.
- [30] Klinder, T., Lorenz, C., Ostermann, J., 2010. Prediction framework for statistical respiratory motion modelling. In: *Proceedings of Medical Image Computing and Computer-Assisted Interventions (MICCAI)*, 327–334.
- [31] Isaksson, M., Jalden, J., Murphy, M.J. On using an adaptive neural network to predict lung tumor motion during respiration for radiotherapy applications, 2005. *Medical Physics* 32, 3801–3809.
- [32] King, A.P., Rhode, K.S., Razavi, R.S., Schaeffter, T.R., 2009. An adaptive and predictive respiratory motion model for image-guided interventions: theory and first clinical application. *IEEE Transactions on Medical Imaging* 28, 2020–2032.
- [33] Geneser, S., Hinkle, J., Kirby, R., Wang, B., Salter, B., Joshi, S., 2011. Quantifying variability in radiation dose due to respiratory-induced tumor motion. *Medical Image Analysis* 15, 640–649.

- [34] Li, T., Thorndyke, B., Schreibmann, E., Yang, Y., Xing, L., 2006. Model-based image reconstruction for four-dimensional PET. *Medical Physics* 33(5), 1288–1298.
- [35] Odille, F., Cindea, N., Mandry, D., Pasquier, C., Vuissoz, P.A., Felblinger, J., 2008. Generalized MRI reconstruction including elastic physiological motion and coil sensitivity encoding. *Magnetic Resonance in Medicine* 56, 1401–1411.
- [36] Odille, F., Vuissoz, P.A., Marie, P.Y., Felblinger, J., 2008. Generalized reconstruction by inversion of coupled systems (GRICS) applied to free-breathing MRI. *Magnetic Resonance in Medicine* 60, 146–157.
- [37] Ernst, F., Bruder, R., Schlaefer, A., Schweikard, A., 2011. Correlation between external and internal respiratory motion: a validation study. *International Journal of Computer Assisted Radiology and Surgery*.
- [38] Fayad, H., Pan, T., Roux, C., Rest, C.C.L., Pradier, O., Visvikis, D., 2009. A 2D-spline patient specific model for use in radiation therapy. In: *Proceedings International Symposium on Biomedical Imaging (ISBI)* 590–593.
- [39] McClelland, J.R., Chandler, A.G., Blackall, J.M., Ahmad, S., Landau, D., Hawkes, D.J., 2005. 4D motion models over the respiratory cycle for use in lung cancer radiotherapy planning. In: *Proceedings SPIE Medical Imaging*.